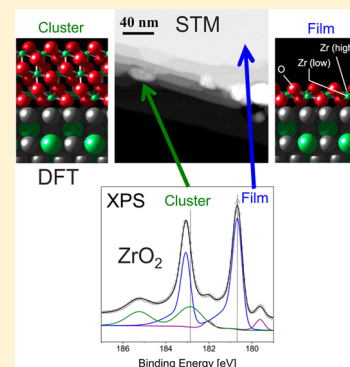Article

Growth of an Ultrathin Zirconia Film on Pt₃Zr Examined by High-Resolution X-ray Photoelectron Spectroscopy, Temperature-Programmed Desorption, Scanning Tunneling Microscopy, and Density Functional Theory

Hao Li,[†] Joong-Il Jake Choi,[‡] Wernfried Mayr-Schmölzer,[‡,§] Christian Weilach,[†,‖] Christoph Rameshan,[†] Florian Mittendorfer,[‡,§] Josef Redinger,[‡,§] Michael Schmid,[‡] and Günther Rupprechter*,[†]

[†]Institute of Materials Chemistry, Vienna University of Technology, 1060 Vienna, Austria

[‡]Institute of Applied Physics and [§]Center for Computational Materials Science, Vienna University of Technology, 1040 Vienna, Austria

ABSTRACT: Ultrathin (∼3 Å) zirconium oxide films were grown on a single-crystalline Pt₃Zr(0001) substrate by oxidation in 1×10^{-7} mbar of O_2 at 673 K, followed by annealing at temperatures up to 1023 K. The ZrO_2 films are intended to serve as model supports for reforming catalysts and fuel cell anodes. The atomic and electronic structure and composition of the ZrO_2 films were determined by synchrotron-based high-resolution X-ray photoelectron spectroscopy (HR-XPS) (including depth profiling), low-energy electron diffraction (LEED), scanning tunneling microscopy (STM), and density functional theory (DFT) calculations. Oxidation mainly leads to ultrathin trilayer (O−Zr−O) films on the alloy; only a small area fraction (10−15%) is covered by ZrO_2 clusters (thickness ∼0.5−10 nm). The amount of clusters decreases with increasing annealing temperature. Temperature-programmed desorption (TPD) of CO was utilized to confirm complete coverage of the Pt₃Zr substrate by ZrO_2, that is, formation of a closed oxide overlayer. Experiments and DFT calculations show that the core level shifts of Zr in the trilayer ZrO_2 films are between those of metallic Zr and thick (bulklike) ZrO_2. Therefore, the assignment of such XPS core level shifts to substoichiometric ZrO_x is not necessarily correct, because these XPS signals may equally well arise from ultrathin ZrO_2 films or metal/ZrO_2 interfaces. Furthermore, our results indicate that the common approach of calculating core level shifts by DFT including final-state effects should be taken with care for thicker insulating films, clusters, and bulk insulators.

1. INTRODUCTION

Zirconia (ZrO_2) is widely used in heterogeneous catalysis and is known as an excellent support (e.g., for Ni nanoparticles of reforming catalysts) and as a catalyst itself, due to its favorable chemical and mechanical stability.[1] However, molecular mechanisms of the functionality of ZrO_2 and, in particular, of the oxide−metal interface need to be better understood. In order to conduct fundamental studies on ZrO_2 via surface-science methods, an approach that has been successfully applied to various other oxides,[2−4] it is required to prepare and thoroughly characterize a model zirconia support. However, single-crystal (bulk) ZrO_2 exhibits poor electrical conductivity and is prone to charging, which usually hinders application of many surface-science techniques.[5] In order to overcome this problem, ultrathin ZrO_2 films are prepared on a conducting substrate.

One way of growing such ultrathin films is to deposit and oxidize zirconium (Zr) on a suitable single-crystal substrate, resulting, for example, in the epitaxial growth of (111) oriented films with cubic fluorite structure.[6−9] However, scanning tunneling microscopy (STM) images of these films typically revealed ZrO_2 films with nonuniform thickness, containing a substantial amount of defects.[6] Furthermore, Zr evaporation is

rather difficult and slow due to its high melting temperature and low vapor pressure at the melting point.

Recently, an alternative route to ultrathin ZrO_2 films via oxidation of a Pt₃Zr(0001) alloy single crystal has been reported by Antlanger et al.[10] Owing to the strong bond between Pt and Zr and the fact that Pt is more inert to oxidation than Zr, the oxidation process is rather slow, which is very favorable for growing ordered ultrathin films. After postannealing, a planar oxide film consisting of an O−Zr−O trilayer was observed by STM.[10]

In order to further examine and better understand the mechanism of formation and structure of ultrathin ZrO_2 films grown on a Pt₃Zr(0001) single crystal, we applied (synchrotron-based) X-ray photoelectron spectroscopy (XPS), combined with density functional theory (DFT) calculations, to study and identify the core level shifts of the oxidic Zr species. Furthermore, we have used carbon monoxide (CO) as a probe molecule to investigate the continuity of the oxide films by performing temperature-programmed desorption (TPD). Low-
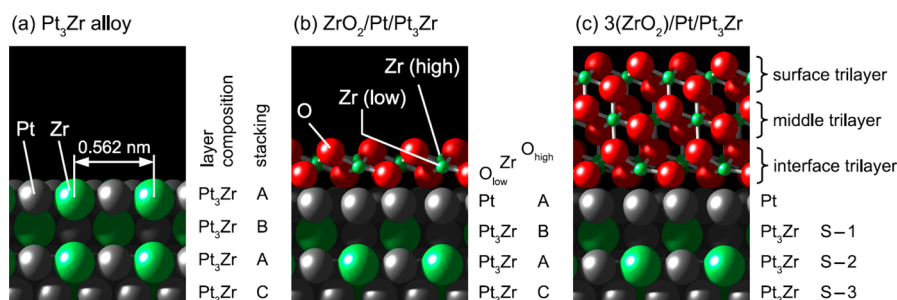
Figure 1. Side views of (a) Pt₃Zr substrate and (b) structure of the trilayer oxide film. (c) Three-trilayer film used for core level calculations, together with layer designations.

energy electron diffraction (LEED) and STM were used to study the growth and structure of the oxide.

2. EXPERIMENTAL AND COMPUTATIONAL METHODS

In order to prepare a model zirconia thin film, a Pt₃Zr(0001) single crystal was cleaned by sputtering (8×10^{-6} mbar of Ar, 2 kV) at room temperature (20 min), annealing in ultrahigh vacuum (UHV) at 1173 K (10 min), sputtering (20 min) during cooling from 673 to 373 K, and finally annealing in UHV at 1173 K (10 min). After cleaning, the Pt₃Zr(0001) single crystal was exposed to 1×10^{-7} mbar of O_2 at 673 K for 30 min, followed by annealing in UHV at 1023 or 1073 K for 20 min. This procedure follows the recipe in the work of Antlanger et al.,[10] but the final annealing temperatures are at the lower end of the range given there (up to 1173 K).

Synchrotron-based high-resolution XPS measurements were carried out at beamline I511 at the MAX II electron storage ring (Lund), which is a soft-X-ray beamline equipped with a modified SX-700 monochromator for high photon energy resolution. Details of this setup can be found elsewhere.[11] In short, the system consists of two UHV chambers with base pressures of ~5×10^{-10} mbar. The preparation chamber is equipped with a sputter gun and LEED (4-grid optics), which was used for cleaning the sample surface and to control surface structure, respectively. The analysis chamber is equipped with a Specs Phoibos 150 NAP (near ambient pressure) analyzer. The binding energy of photoelectron peaks was calibrated by measuring the Fermi edges. The program XPSPEAK was used to conduct peak deconvolution and Shirley background subtraction. The Zr 3d spectra and O 1s spectra were fitted by use of Gauss−Lorentz sum functions with asymmetric peak shape [described by the parameters named TS (peak shape asymmetry) and TL (tail extension asymmetry)]. The shapes and full width at half-maximum (fwhm) have been fixed and propagated along the series of spectra.

The laboratory measurements were performed in two separate UHV chambers, with LEED being used to confirm analogous sample preparation. The STM measurements were performed in a UHV chamber, attached to another UHV preparation chamber for sputtering and annealing.[10] The STM images were acquired at room temperature by use of electrochemically etched tungsten tips. The bias voltage values given are sample voltages (positive bias means tunneling into the unoccupied state of the sample surface). Depending on the sample surface, the tunneling voltages were kept around ±0.1 V for high resolution on large and flat terraces, whereas low tunneling current (<0.1 nA) and high bias voltages (≈−6 V) were used for imaging surfaces with clusters, in order to minimize tip crashes. The TPD experiments were performed in

another UHV chamber (also equipped with LEED and XPS) with a base pressure of 5×10^{-10} mbar.[12,13] TPD spectra were collected by a differentially pumped MKS eVision+ quadrupole mass spectrometer, and temperature ramping was performed by a Eurotherm 3216 PID controller, with a heating rate of 60 K/min.

The DFT calculations were performed with the Vienna Ab-Initio Simulation Package (VASP), using a projector augmented wave (PAW) formalism[14,15] and an energy cutoff of 400 eV. The Brillouin zone integration was performed with an automatically generated Gamma-centered $12 \times 12 \times 1$ Monkhorst−Pack k-point mesh.[16] As a previous study had shown that the inclusion of van der Waals contributions is crucial for an appropriate description of the oxide−substrate interface,[10] the calculations were performed with the optB88 van der Waals density functional (vdW-DF).[17] The core levels shifts were determined in the final state approximation.[18] In these calculations, originally designed for metallic systems, a core electron is removed and added to the delocalized states above E_F. It should be noted that the current implementation[18] does not allow an evaluation of the absolute positions of the core levels, but rather only the relative changes with respect to a reference structure.

The model cells for the calculations are similar to the ones described before,[10] using a $(\sqrt{3} \times \sqrt{3})$ model cell to mimic the experimentally found $(\sqrt{19} \times \sqrt{19})$ superstructure. The oxide film was placed on a 9-layer-thick alloy substrate slab with an ABACABACA stacking. At the alloy−oxide interface, the Zr atoms in the A-type layer were replaced by Pt to simulate the Pt termination found in the experiments;[10] see Figure 1b,c. Concerning the oxide overlayer, one Zr atom of the oxide film was positioned on top of a substrate Pt atom to which it binds.[10] The two other Zr atoms of the oxide in the cell buckle up [marked as Zr(high) in Figure 1b] and do not bond to the substrate. This choice of a unit cell should allow the simulation of the most extreme cases of different Zr sites; other configurations also present in the large experimental unit cell will have their Zr atoms somewhere in between.

To keep the computational effort reasonable, the unit cell of the DFT model is much smaller than the experimental one and therefore has a slightly different ratio between the in-plane lattice constants of the oxide and substrate. Similar to our approach in another study,[19] we have therefore used two DFT models: model 1 has the DFT value of the substrate lattice constant but the oxide compressed to an in-plane lattice constant of 0.33 nm,[10] and model 2 uses the experimental lattice constant of the oxide film (0.35 nm) but an expanded substrate. Out-of-plane relaxation was allowed in all cases. For the calculation of the core level shifts, we have used model 1 for

the substrate and model 2 for the oxide. This means that the core level shifts were always calculated for atoms in a layer with its natural in-plane lattice constant.

3. RESULTS AND DISCUSSION

3.1. Trilayer Oxide: LEED and CO-TPD. The atomic surface structure of the Pt_3Zr alloy and of the thin oxide film were already reported in the study of Antlanger et al.[10] Pt_3Zr forms an ordered alloy and crystallizes in the Ni_3Ti ($D0_{24}$) structure, which can be considered as a hybrid of face-centered cubic and hexagonally close-packed structures, with an in-plane lattice constant of $a = 0.562$ nm and 2×2 surface atoms in this unit cell. The oxide film consists of an O−Zr−O trilayer, which has an in-plane lattice constant of 0.350 nm. In addition, the consumption of Zr when growing the oxide results in at least one pure Pt(111) layer beneath the oxide (lattice constant of $\approx$0.28 nm), as shown schematically in Figure 1b.

The LEED images in Figure 2 show the electron diffraction pattern of the clean $Pt_3Zr(0001)$ substrate as well as of the
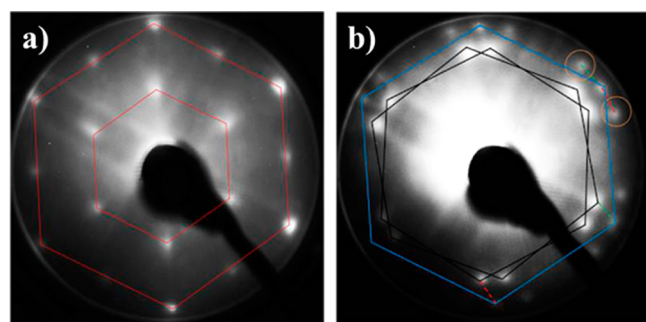

Figure 2. Diffraction patterns obtained from (a) clean Pt_3Zr (0001) and (b) Zr oxide film. Both patterns were acquired with an electron energy of 80 eV.

model zirconium oxide film after oxidation and postannealing. The LEED pattern of the clean alloy (Figure 2a) clearly exhibits a hexagonal lattice: both first-order diffraction spots (corresponding to the 0.56 nm alloy cell; inner hexagon in Figure 2a) and second-order spots (vertices of the outer hexagon) can be observed. After oxidation and postannealing (Figure 2b), the inner hexagon disappears, whereas the outer hexagon seems to remain. As mentioned, oxidation leads to the accumulation of pure Pt(111) at the interface, with a lattice constant of 0.28 nm, half of the lattice constant in the alloy. Therefore, the outer hexagon (blue) in Figure 2b can be assigned to the Pt(111) beneath the oxide. In addition, two additional hexagons of LEED spots appear (black lines in Figure 2b). Their lattice constant is 1.25 times that of Pt(111) and the rotation angle is $\approx$6° relative to Pt(111). These values are in line with the previous STM results (rotation angle ±6.8°),[10] and thus the two hexagons correspond to two rotational domains of the oxide. Also, additional spots could be observed, two of them indicated by orange circles. Such spots are assigned to a moiré pattern caused by the superposition of the Pt(111) and the zirconium oxide lattice. In Figure 2b, two moiré vectors are shown as difference vectors (red and green dashed lines) between the reciprocal-space vectors of Pt(111) and ZrO_2 spots, and the two moiré spots marked by orange circles can be explained by adding the moiré vectors to a first-order spot of the Pt(111) lattice.

One important issue regarding the growth of a thin film oxide on a substrate is its continuity. For systematic adsorption/reactivity studies the model oxide should entirely cover the substrate, so that the interpretation is not complicated by signals resulting from the bare substrate. Extended STM studies have indicated complete coverage, but this should be corroborated by an integral method such as TPD with CO as probe molecule.

CO adsorption on Pt or Pt alloys has been studied in detail, and excellent reference data exist.[20−23] On the clean Pt(111) surface, CO-TPD features a broad main peak at around 450 K, shifting to 410 K upon increasing the exposure, assigned to desorption from large and smooth terraces. CO desorption from steps produces a small hump around 500 K; even at highly stepped surfaces, this signal reaches saturation already at an exposure of about 0.5 langmuir (L).[22] Figure 3 shows a CO
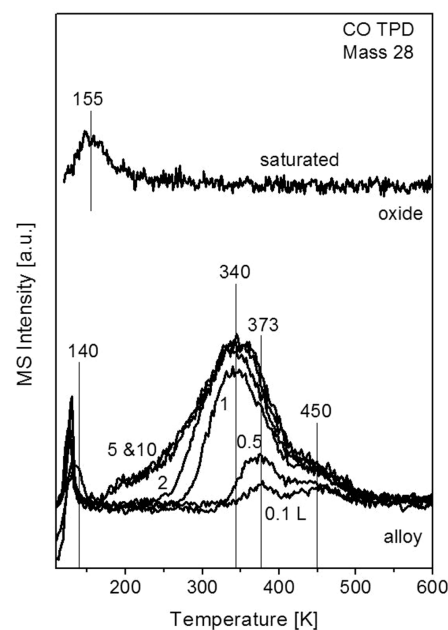

Figure 3. CO-TPD spectra of (bottom) clean Pt_3Zr alloy (0.1, 0.5, 2, 5, and 10 L of CO dosed at 90 K) and (top) Zr-oxide covered Pt_3Zr (after cooling in 1×10^{-6} mbar of CO from 300 to 120 K) .

dosage series of TPD spectra on the alloy and on the oxide (desorption below 140 K results from CO desorbing from the Ta heating wires). In case of the alloy, at 0.1 and 0.5 L exposure a main species at around 373 K and a broader feature around 450 K are observed. As the exposure increases to 1 L, the main species grows and shifts to 340 K (due to intermolecular repulsion weakening the binding energy), similar to the behavior of CO desorption from large planar Pt(111) terraces. In contrast, the high-temperature 450 K shoulder is unaffected, like CO adsorption on the steps of Pt(111). We thus attribute the main 373/340 K peak to CO desorption from Pt atoms in the alloy and the small shoulder to CO desorption from Pt atoms at defects/steps.

Higher exposures (2, 5, and 10 L) broaden (but do not shift) the main peak and also produce a low-temperature shoulder, which might be related to CO at Zr sites ($^1/_4$ of all surface atoms).

The adsorption energy was also estimated by applying the Redhead equation.[24] A pre-exponential factor for desorption of 10^{13} s^{-1} was used. For the alloy, the desorption maximum at a

temperature of 340 K corresponds to a desorption energy of $E_{TPD} \approx 0.91$ eV.

For the oxide annealed at 1073 K, after saturation with CO its desorption was observed at 155 K (topmost trace in Figure 3; there was no desorption from the oxidized heating wires), which corresponds to a desorption energy of ≈0.42 eV (again assuming a preexponential factor of 10^{13} s^{-1}). DFT calculations confirm the weak physisorption of the CO molecule on the ZrO$_2$ trilayer film. In the most favorable configuration, the molecule adsorbs above the Zr atoms of the oxide layer in an upright position, with a Zr–C distance of 0.25 nm and an adsorption energy of 0.59 eV. When the error bars of DFT for CO adsorption[25] as well as the simplified analysis of the experimental data are considered, this value is consistent with the experimental result. Altogether, this clearly proves that the alloy substrate is fully covered by the thin oxide film, and no Pt$_3$Zr or Pt is exposed at the solid–vacuum (or solid–gas) interface.

3.2. Core Level Shifts: Two Oxide Species. The growth of the oxide on Pt$_3$Zr was also monitored by synchrotron-based HR-XPS, as shown in Figure 4 and Table 1. The spectra were
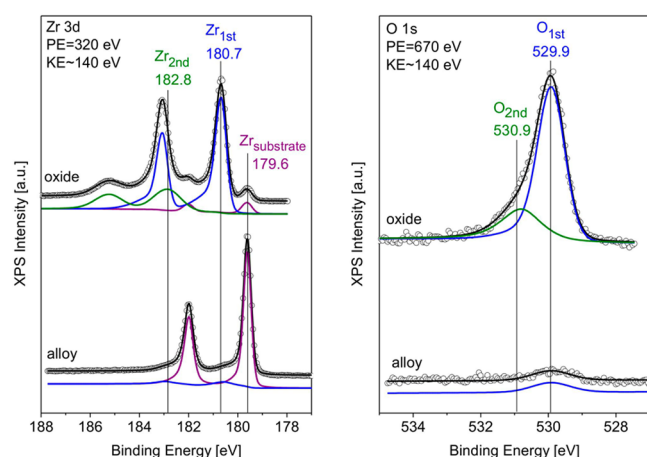

Figure 4. (Left) Zr 3d and (right) O 1s XP spectra of clean alloy and of the oxide annealed at 1023 K (spectra taken at 300 K, kinetic energy ≈140 eV).

Table 1. Summary of Literature Values and Our Results for Binding Energy of Zr 3d$_{5/2}$ Levels for Zr and Zr Oxides

	Zr 3d$_{5/2}$ binding energy, eV	ref
Substrates (Bulk)		
pure Zr (single crystal)	178.6	27
Pt$_3$Zr	179.6	this work
ZrO$_2$ (Thicker Layer)		
ZrO$_2$ (oxidation of Zr single crystal)	183.1	27
ZrO$_2$ grown by PVD on Pt(111)	182.9	9
Trilayer ZrO$_2$/Pt/Pt$_3$Zr		
Zr$_{first}$ (oxidation of Pt$_3$Zr)	180.7	this work
Zr$_{second}$ (oxidation of Pt$_3$Zr)	182.8	this work

recorded at normal emission with photon energies of 320 and 670 eV for the Zr 3d and O 1s ranges, respectively, yielding in both cases photoelectrons with a kinetic energy of ~140 eV. With that kinetic energy, only the photoelectrons from the topmost surface layers escape. By use of NIST Standard Reference Database 71,[26] the inelastic mean free path (IMFP)

for ZrO$_2$ corresponding to 140 eV is 0.54 nm; that is, mainly the first two layers are probed. The Zr 3d spectrum of the clean alloy exhibits a pronounced doublet at 179.6 and 182.0 eV due to Zr 3d$_{5/2}$ and Zr 3d$_{3/2}$, respectively. In addition, another doublet with much lower intensity was observed at 180.7 and 183.1 eV. Almost no signal could be detected in the O 1s region; thus the doublet with higher intensity is assigned to metallic Zr in Pt$_3$Zr, whereas the small features were assigned to Zr bound to residual oxygen. For comparison with pure Zr, we will use the value of 178.6 eV reported for a Zr(0001) single crystal;[27] thus the alloyed Zr is shifted to higher binding energy (BE) by +1.0 eV.

After oxidation at 673 K and postannealing at 1023 K, the signal of metallic (alloyed) Zr from the substrate (Zr$_{substrate}$) could still be observed, although strongly attenuated by the oxide and interfacial Pt. However, the Zr 3d spectrum now also displays two doublets, originating from two different oxidic species (Zr$_{first}$ and Zr$_{second}$).

Detailed peak deconvolution shows that the main peak Zr$_{first}$ is located at 180.7 eV (Zr 3d$_{5/2}$), shifted by +2.1 eV relative to pure Zr. As will be shown, according to STM and DFT this species can be assigned to the O–Zr–O trilayer oxide. In contrast, the smaller Zr$_{second}$ species is positioned at 182.8 eV, shifted by +4.2 eV with respect to pure Zr. This position is characteristic of bulk ZrO$_2$ (around 183 eV), as indicated by experiments.[28,31] The shift between Zr$_{first}$ and Zr$_{second}$ is 2.1 eV and the ratio of the intensities is 3:1, based on the integration of the peak areas. In the O 1s region we also observe two species: the main peak (O$_{first}$) is located at 529.9 eV, with a shoulder (O$_{second}$) at approximately 530.9 eV, and the ratio of the intensities is again 3:1. Concerning XPS peak fitting, note that asymmetry (high-energy tail) is induced by many-body interactions of photoelectrons with free electrons at the Fermi edge. The ultrathin oxide film has a well-defined Fermi edge (like a metal), and thus Zr$_{first}$ exhibits asymmetry, whereas the electron density around the Fermi level of the more insulating clusters is much less, leading to symmetric Zr$_{second}$.

XPS studies of thin Zr oxide layers grown by oxidation of metallic Zr (Zr single crystals and polycrystalline foil) were reported in the literature.[27−29] For oxides of several-nanometer thickness, Zr^{4+} generally shifts ∼+4.5 eV relative to metallic Zr, whereas binding energy shifts of +2.5 to +3.5 eV were attributed to suboxide (formed upon exposure to low O$_2$ amounts).[27,28] An exact identification of the different oxide components has, however, not yet been achieved. Gao et al.[9] applied XPS to study the growth of ZrO$_2$ film on Pt(111) by vapor deposition of zirconium in an oxygen atmosphere (10^{-7} Torr). They also observed a Zr 3d$_{5/2}$ binding energy of 182.9 eV corresponding to bulklike ZrO$_2$ up to ≈5 ML; an additional shift of +0.7 eV at higher thickness (8.3 ML) was attributed to surface charging due to the poor oxide conductivity.[9] As the substrate Pt line was also reported to be shifted by about the same amount, this additional shift is questionable.

In summary, Zr$_{second}$ has similar binding energy as Zr^{4+} species reported in the literature, whereas the large Zr$_{first}$ peak has a binding energy similar to the literature value attributed to Zr suboxide. These values have been summarized in Table 1.

In order to determine the stoichiometry of the ultrathin oxide grown on the Pt$_3$Zr substrate, the following equation is used:

$$\frac{N_{Zr}}{N_O} = \left(\frac{I_{Zr}}{\sigma_{Zr}F_{Zr}}\right)\left(\frac{\sigma_O F_O}{I_O}\right)$$

I represents the intensities of photoelectrons; σ represents the cross section of atoms, taken from the published atomic subshell photoionization cross sections;[30] and F_x represents the flux of incident photons, given by the flux calibration for the I511 beamline in MAX-lab. Specifically, σ_{Zr} and σ_O are 4.259 and 0.313 Mb,[30] and F_{Zr} and F_O were 1.47×10^{13} and 4.36×10^{12} photons/s in our experiment. The calculation results in a Zr/O ratio of 0.55 (1:1.82) for both oxidic species. Within the accuracy expected for such a calculation, this result fits the Zr/O ratio of 0.50 in ZrO_2. Thus, both of the oxidic species should be assigned to ZrO_2 rather than to a suboxide.

As mentioned above,[9] the increase of binding energy with increasing thickness of ZrO_2 films (between 5.2 and 8.3 ML average film thickness deposited on Pt) has been attributed to surface charging. If charging would play a significant role in our experiments, it should be much more pronounced in the synchrotron-based experiments, where the photon flux (and hence the current of photoelectrons leaving the sample) is high, compared to experiments with a laboratory X-ray source. However, we did not find any difference between the core level shifts of our synchrotron and laboratory measurements (the latter with an Al Kα source operated at 300 W). Thus, we exclude charging as a reason for the different "first" and "second" components of the ZrO_2 spectra.

To examine the two oxide features in more detail, we have also performed XPS depth profiling by varying the incident excitation energy, in order to determine the thickness of the two oxidic species (Figure 5). The incident photon energies
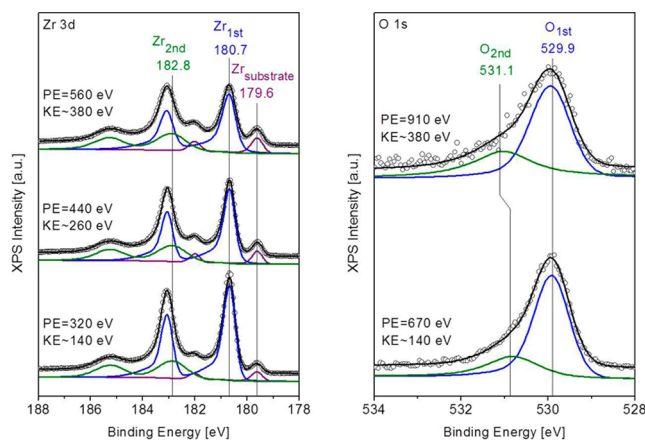

Figure 5. (Left) Zr 3d and (right) O 1s XP spectra of the oxide at different kinetic energies of the photoelectrons (spectra taken at 300 K).

were 320, 440, and 560 eV for Zr 3d, leading to kinetic energies of photoelectrons of 140, 260, and 380 eV, respectively. The corresponding IMFP are 0.54, 0.72, and 0.90 nm, respectively.[26] For O 1s, measurements were taken at 670 and 910 eV (kinetic energy of 140 and 380 eV, respectively).

As a result, the signal for $Zr_{substrate}$ rises with increasing kinetic energy (increasing probing depth), and consequently the relative intensities of both Zr_{first} and Zr_{second} decrease (Figure 6). However, with increasing probing depth, the higher binding energy component Zr_{second} decreases less in intensity than Zr_{first} does, thus the ratio Zr_{first}/Zr_{second} decreases; that is,
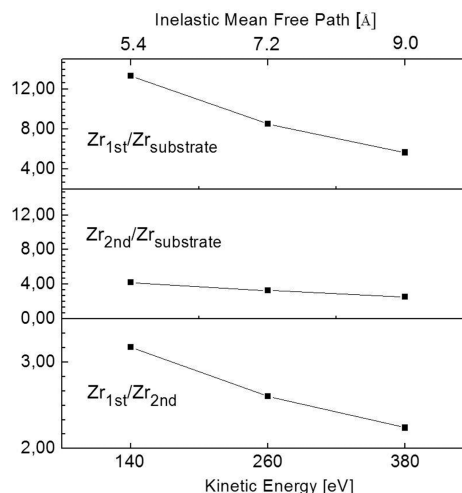

Figure 6. Ratio between different Zr species for kinetic energies of the photoelectrons of 140, 260, and 380 eV.

Zr_{second} is more "three-dimensional". In the O 1s region, the ratio O_{first}/O_{second} also decreases with probing depth (from 3.04 to 1.95). Thus, it is clear that Zr_{second} is "thicker" than Zr_{first}, meaning that the former grows three-dimensionally whereas the latter is more planar.

Obviously, we produced two stoichiometric ZrO_2 types of the same Zr/O ratio but with different thickness and binding energies. Our data suggest that Zr_{first} corresponds to the surface oxide trilayer film whereas Zr_{second} belongs to a thicker "bulk" oxide; in the following we will provide support for this assignment.

Additional information is obtained from the calculated core level binding energy shifts. The DFT calculations reveal a complex pattern for the Zr 3d core levels (Table 2). For the ideal Pt_3Zr bulk alloy substrate, the core levels of the Zr atoms are at significantly higher BE than in pure Zr (+1.25 and +1.46

Table 2. Calculated Core Level Shifts of Zr 3d Levels for Zr and Zr Oxides[a]

	Zr 3d shift, eV	O 1s shift, eV
Substrate (Bulk)		
Pt_3Zr (bulk): A layer	1.25	
Pt_3Zr (bulk): B/C layer	1.46	
Pt-Terminated Pt_3Zr (below the Oxide)		
Zr_{S-1} (B)	1.08	
Zr_{S-2} (A)	1.02	
Zr_{S-3} (C)	1.30	
Trilayer ZrO_2/Pt/Pt_3Zr		
$ZrO_{2,low}$	2.30	0.01
$ZrO_{2,high}$	2.56	−0.01
Three Trilayers $3(ZrO_2)$/Pt/Pt_3Zr		
$ZrO_{2,interface,low}$	2.28	0.05
$ZrO_{2,interface,high}$	2.53	0.37
$ZrO_{2,middle}$	2.69	1.22
$ZrO_{2,surface}$ (lower, higher O layer)	2.83	1.21, 0.89
Bulk ZrO_2		
cubic ZrO_2	2.79	1.45
monoclinic ZrO_2 (3-fold, 4-fold O)	2.79	1.66, 1.30

[a]See Figure 1 for structures and labeling of the layers. For Zr, the bulk of pure hexagonal Zr is taken as a reference (0 eV); for O, the core level shifts are with respect to O in the trilayer oxide.

eV), and the A layer and B/C layers (the latter two are equivalent) differ by 0.2 eV. In the alloy substrate underneath a pure Pt layer and a ZrO_2 trilayer, the shift with respect to Zr is somewhat reduced to ≈1.1 eV, in good agreement with the experimental value of 1.0 eV.

For the supported ZrO_2 trilayer film, the calculations predict a pronounced shift of the Zr 3d levels, which depends on whether the Zr atom is buckled up or down in the film: Core level shifts are +2.30 eV for the lower-lying Zr atoms and +2.56 for the higher atoms. This confirms the experimental assignment of the Zr peak at 180.7 eV (+2.1 eV) to the trilayer oxide. Modeling the interaction of the Pt_3Zr surface with a mesoscopic ZrO_2 cluster is computationally unfeasible, but the comparison with a thicker ZrO_2 film consisting of three O−Zr−O trilayers (Figure 1c) already shows clear trends (Table 2): While the core level shifts of the atoms closest to the substrate are essentially identical to those of the single trilayer, the Zr atoms at a larger distance from the substrate show higher 3d binding energies, with shifts of 2.69−2.83 eV. These values are very close to the calculated core level shifts of bulk ZrO_2 (2.79 eV) and thus confirm that thicker ZrO_2 clusters should have bulklike core level shifts. Nevertheless, the calculated shifts are much less than the experimental ones for the "3D" ZrO_2 (Zr_{second}, +4.2 eV) and bulk ZrO_2.

For oxygen, the O layer at the interface again shows similar core level shifts as in the ultrathin trilayer film, and the upper layers exhibit higher O 1s binding energies. In this "thick" ZrO_2 film, we can also observe a clear surface core level shift for oxygen; the outermost O layer has 0.3 eV lower BE than the O layers in the middle of the oxide. In the middle layers of the ZrO_2 three-trilayer film, also the O 1s core level shifts are close to those of bulk ZrO_2; the values deviate by only 0.1−0.4 eV. For oxygen, the difference between the trilayer film and the middle of the thicker oxide (1.2 eV) is exactly the same value as found experimentally for the thick O_{second} and trilayer O_{first}.

In summary, DFT corroborates the experimental result that the "first" peaks are due to the ultrathin trilayer ZrO_2 film, while the "second" peaks are due to a thicker (bulklike) oxide. There is one point where experiment and DFT disagree, however: The calculated core level shifts of Zr in the "thick" ZrO_2 film and also of bulk ZrO_2 are far too low. The present computational approach (PBE) gives a reasonable description for the supported trilayer but not for most of the thicker ZrO_2 film or bulk ZrO_2. To understand this problem, one has to note that for technical reasons (charge neutrality), in the calculation the photoelectron is not removed from the system but only lifted to an energy at or above the Fermi level.[18] A detailed analysis shows that in the calculation the excited Zr core electron from ultrathin ZrO_2 or the interface of thicker films is delocalized in the metal substrate, whereas in bulk ZrO_2 or the middle and upper layers of the thick films it remains localized at the atom with the core hole. There, this electron (only present in the calculation, not in the real system) leads to additional screening and thereby a smaller core level shift. For oxygen, the extra (calculated) electron is always localized around the core hole, and thus it leads to a constant offset of the core level energy. When calculating differences between the core level shifts for different structures, the error therefore cancels out for oxygen. This effect will be discussed in detail in a forthcoming publication.

Finally, it should be noted that different core level shifts of the ZrO_2 in contact with a metal substrate and of thick (bulklike) ZrO_2 indicate that the electronic structure of the ultrathin zirconia film is influenced by the metallic substrate underneath. It remains to be determined whether this inherent difference between the thin-film model and technological ZrO_2 may affect the adsorption and catalytic properties.

3.3. Influence of Annealing Temperature. Preceding STM studies have shown that a planar oxide-covered surface was obtained after oxidation at 673 K and postannealing above 1023 K,[10] annealing to lower temperatures resulted in many islands. Upon postannealing at 1023 K, our synchrotron XPS results show that the intensity ratio between Zr_{first} and Zr_{second} is 3.2:1. As explained above, Zr_{first} and O_{first} correspond to the trilayer film, whereas Zr_{second} and O_{second} should be assigned to a thicker component, that is, ZrO_2 clusters. Thus, no homogeneous trilayer oxide is formed after annealing at 1023 K, whereas STM indicates a homogeneous oxide after annealing at higher temperatures, up to the point where the oxide decomposes (>1173 K).[10] This means that the surface state after oxidation strongly depends on the postannealing temperature. Therefore, a combined study by synchrotron XPS and STM of the oxides *before and after annealing at different temperatures* should enable us to better understand the formation and morphology of the ZrO_2 ultrathin film and the ZrO_2 clusters as a function of the postannealing temperature.

After oxidation at 673 K, the Zr 3d spectrum exhibits both the metallic (alloy) Zr signal of the substrate underneath and broad peaks of oxidic species Zr_{oxide} (Figure 7). Zr_{oxide} is shifted
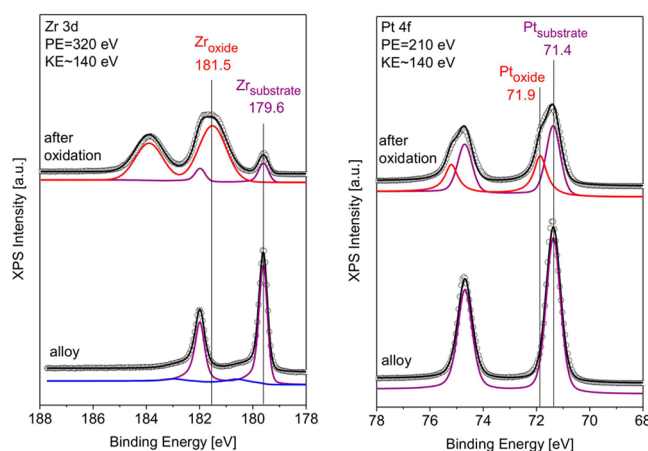

Figure 7. (Left) Zr 3d and (right) Pt 4f XP spectra of clean alloy and oxide prepared by oxidation of alloy at 673 K in 1×10^{-7} mbar of O_2 for 30 min (spectra taken at 300 K, kinetic energy ≈140 eV).

by +2.9 eV relative to pure Zr. This shift is larger than that of ZrO_2 film ($Zr_{first(film)}$, +2.1 eV) but smaller than that of ZrO_2 clusters ($Zr_{second(cluster)}$, +4.2 eV). Furthermore, analysis of the stoichiometry revealed a Zr/O ratio of 0.2 (1:5). Likewise, the Pt 4f spectrum shows both the metallic (alloy) Pt signal ($4f_{7/2}$ at 71.4 eV) and an additional oxidic species (Pt_{ox}), which is shifted by +0.5 eV relative to alloy Pt. It is known that O_2 can dissociate on Pt(111) above 160 K[32] and it can form PtO-like and PtO_2-like surface oxides.

Chemisorbed oxygen induces a shift of ∼0.6 eV of the Pt 4f peak relative to surface metallic Pt[33,34] (i.e., from 70.5 to 71.1 eV). For various surface oxide phases, higher Pt 4f binding energies are reported at around ∼72.3 eV.[35,36] The Pt_{ox} peak in our study (71.9 eV) therefore lies between the peaks of chemisorbed O on the Pt(111) surface (∼71.1 eV) and those of heavily oxidized PtO_x surface oxides (∼72.3 eV). When it is

considered that Zr also affects the Pt BE, the identification of the PtO_x signal must remain uncertain, but the relatively low chemical potential of oxygen ($\mu_O = -1.37$ eV) at 10^{-7} mbar of O_2 and 673 K is probably outside the stability range of any Pt surface oxides. Together with the observation of islands by STM,[10] our results imply that the oxidation of Pt_3Zr leads to an intermediate state, disordered ZrO_x islands. The high O/Zr ratio and the Pt 4f spectra indicate additional oxygen binding to Pt, for example, at the interface or in the form of O dissolved in near-surface layers of the substrate.

When the thin oxide film was then postannealed at 923 K, the two distinct ZrO_2 species ($Zr_{first(film)}$ and $Zr_{second(cluster)}$) were already formed (Figure 8) and the Pt_{ox} signal vanished

Figure 9. Ratio between $Zr_{first(film)}$ and $Zr_{second(cluster)}$ after annealing at 923, 973, and 1023 K.
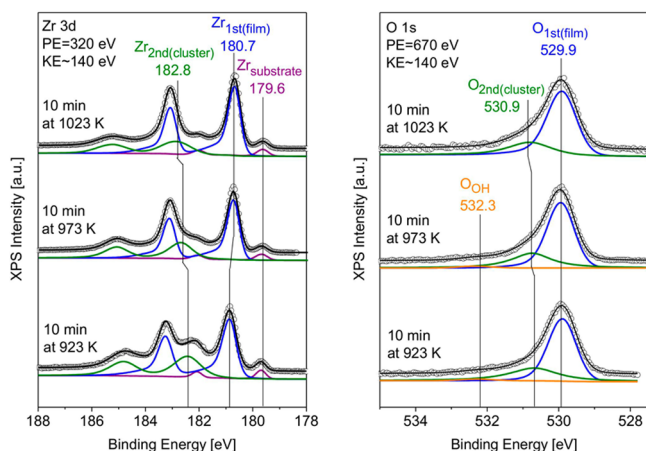

Figure 8. (Left) Zr 3d and (right) O 1s XP spectra of oxide formed at 673 K, postannealed at 923, 973, and 1023 K (spectra taken at 300 K, kinetic energy ≈140 eV).

(spectrum not shown). The intensity of the total oxidic Zr signal increased, whereas the total O signal remained unchanged. Apparently, postannealing in ultrahigh vacuum pulled up more Zr atoms from the alloy substrate underneath, entering the surface layer and reacting with the excess oxygen created by breaking Pt–O bonds, forming ZrO_2 (as indicated by the same Zr/O ratio as obtained at higher T for both film and clusters). If the amount of ZrO_2 is too high to be accommodated in a trilayer oxide film, the remaining ZrO_2 will form clusters.

XPS also shows that postannealing at 923 K results in a $Zr_{first(film)}/Zr_{second(cluster)}$ ratio of 2:1, which increases to 2.4:1 upon postannealing at 973 K and further increases to 3.2:1 as the postannealing temperature reaches 1023 K (Figure 9).

In contrast, the $Zr_{first(film)}/Zr_{substrate}$ ratio does not change significantly with increasing postannealing temperature, staying around 13.0. Assuming that the clusters are thick enough to block the $Zr_{substrate}$ signal, this indicates that any retreat of the clusters, whether by decomposition or sintering, leads to a trilayer film in the remaining area; that is, all the area initially covered by clusters is then covered by the trilayer film, as already indicated by our TPD data.

To properly fit the O 1s spectra in Figure 8, a very weak component at 532.3 eV was included. Most likely, this is due to minute amounts of OH groups because C 1s did not indicate any carbon so that (adventitious) C–O containing species can be excluded. In any case, this feature was extremely weak.

In order to directly prove the coexistence of the trilayer film and oxide clusters, as well as to examine the influence of
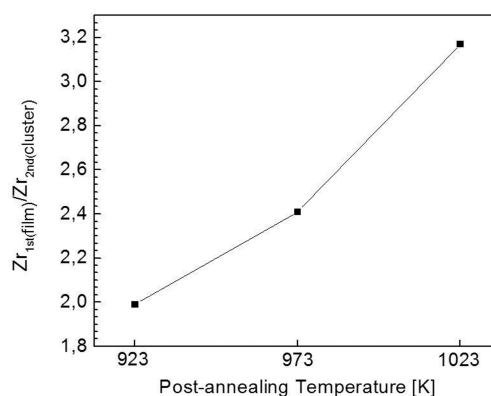
annealing temperature on oxide morphology, corresponding STM images of oxide annealed at different temperatures were recorded. The STM images in Figure 10 show that the surfaces
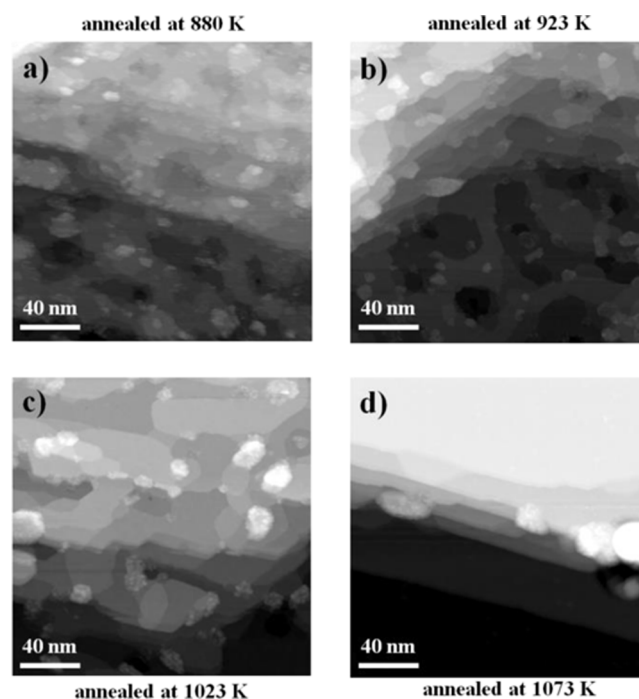

Figure 10. STM images of the oxide annealed at (a) 880 K, (b) 923 K, (c) 1023 K, and (d) 1073 K. The brightness of terraces represents the height, and the bright patches are the oxide clusters.

annealed at 880 and 923 K exhibit many clusters with 5−20 nm diameter. Their mottled or scratchy appearance indicates interaction with the tip, probably because they are poorly conducting. It is known that the ultrathin trilayer oxide already shows a large band gap,[10] and tunneling is only possible due to the small thickness. Thus, it is not unexpected that large ZrO_2 clusters, which should be chemically similar to bulk ZrO_2, are insulating with a large band gap.

It is almost impossible to obtain STM images of clusters higher than ∼3 nm. The apparent height of the oxide clusters varies from ∼0.5 nm to >3 nm. For an insulator, the actual height is larger than the apparent height.[37] For Figure 10, we have selected images where the tip was stable (i.e., the tip was not destroyed or strongly modified while scanning); thus they

show only clusters with <3 nm height. Most of the clusters are located at steps; that is, more clusters are observed when there are more steps.

At higher annealing temperature (1023 and 1073 K) the oxide clusters decrease in number; especially the smallest clusters disappear. When the oxide is annealed at 1073 K, large terraces (up to ≈100 nm) can be obtained. Almost no small clusters (height ~1 nm) can be observed, and the number of large clusters (height >3 nm) strongly decreased.

According to XPS, the $Zr_{first(film)}/Zr_{second(cluster)}$ ratios corresponding to the preparation conditions of Figure 10 b and c are 2.4, and 3.2 respectively. As the trilayer film is much thinner than the clusters, the ratio of the surface area covered by the trilayer film and the clusters is different from the XPS intensity ratio (the trilayer film produces less intensity per area). In the following we assume that the trilayer film has the thickness of a $ZrO_2(111)$ trilayer in the bulk (0.295 nm), while the clusters are much thicker than the inelastic mean free path (0.54 nm). This yields an area fraction for the clusters of 15% and 12% for annealing at 923 and 1023 K, respectively. It is difficult to estimate the areas of thick oxide clusters from our STM images (there are also islands covered by the trilayer oxide due to Zr mass transport; see ref 10), but we find that roughly 15% of the area is covered by thick oxide clusters in Figure 10 a,b. Considering that the cluster density strongly depends on the local step density of the crystal, and that we have to avoid areas with large clusters for stable imaging by STM, this level of agreement is better than what could be expected.

We should mention that the cluster density further decreases upon annealing to higher temperatures (the sample heater used at the synchrotron only allowed 1073 K). In the annealing temperature range used for most of our STM studies (1140−1173 K[10]), we do not find any oxide clusters except in very rough or highly stepped areas of the crystals. At even higher temperatures, in some areas the oxide disappears; given the strong Zr−O bonds and the low vapor pressure of ZrO_2, the only explanation is the dissolution of oxygen in the Pt_3Zr substrate. This observation is also a clue to why the oxide clusters disappear when the sample is annealed: With increasing temperature, more and more oxygen dissolves in the substrate. Since the substrate is Zr-depleted after formation of the oxide, the remaining Zr is easily accommodated in the substrate as well.

This explanation also suggests that the trilayer ZrO_2 film is thermodynamically more favorable than thick ZrO_2 clusters on the surface. This essentially means that ZrO_2 grows in Stranski−Krastanov mode: First the trilayer oxide forms, and then the extra material creates 3D clusters. Some of us have recently suggested the same for ZrO_2 grown on Pd_3Zr.[19] Upon dissolution of oxygen, the reverse sequence happens: First the 3D clusters disappear, and then the (more favorable) 2D trilayer begins to dissolve.

4. CONCLUSIONS

We have studied the ultrathin ZrO_2 oxide film formed upon oxidation and annealing of a $Pt_3Zr(0001)$ single crystal, employing a combination of (synchrotron) HR-XPS, TPD, LEED, and STM. The experimental studies were complemented by DFT simulations in order to interpret the observed core level shifts. The results indicate that, at moderate annealing temperatures, the oxide overlayer is comprised of a trilayer film (O−Zr−O) as well as of oxide clusters. The two

species have different core level shifts, +2.1 eV for the trilayer film and +4.2 for the clusters (both referenced to pure Zr); the latter have a clearly insulating nature. The oxide clusters decompose upon high-temperature (>1023 K) annealing, resulting in the formation of a continuous trilayer ZrO_2 film that is well-suited as a model support for reforming catalysts or fuel cell anodes.

Our results also indicate that the usual assignment of Zr core level shifts positioned between those of metallic Zr and bulk ZrO_2 to suboxides is not necessarily correct. The ultrathin trilayer oxide clearly has ZrO_2 stoichiometry (with O binding to the Zr, not to the substrate) and a band gap; nevertheless, it would be interpreted as a substoichiometric oxide on the basis of its core level shift. We consider it likely that what has previously been assigned to ZrO_x suboxides on the basis of core level shifts is in many cases instead ultrathin ZrO_2 or the metal/ZrO_2 interface.

■ AUTHOR INFORMATION

Corresponding Author
*E-mail: guenther.rupprechter@tuwien.ac.at.

Present Address
∥Lenzing AG, 4860 Lenzing, Austria.

Notes
The authors declare no competing financial interest.

■ REFERENCES

(1) Tanabea, K.; Yamaguchi, T. Acid-Base Bifunctional Catalysis: An Industrial Viewpoint. *Catal. Today* **1994**, *20*, 185−198.

(2) Freund, H.-J.; Pacchioni, G. Oxide Ultra-Thin Films on Metals: New Materials for the Design of Supported Metal Catalysts. *Chem. Soc. Rev.* **2008**, *37*, 2224−2242.

(3) Kuhlenbeck, H.; Shaikhutdinov, S.; Freund, H.-J. Well-Ordered Transition Metal Oxide Layers in Model Catalysis—A Series of Case Studies. *Chem. Rev.* **2013**, *113*, 3986−4034.

(4) Diebold, U.; Li, S.-C.; Schmid, M. Oxide Surface Science. *Annu. Rev. Phys. Chem.* **2010**, *61*, 129−148.

(5) Lou, J. .; Hess, U.; Mitchell, K. A. R. The Growth of Zirconium Oxide Thin Films on Au(111) Single-Crystal Surfaces. *Appl. Surf. Sci.* **1992**, *62*, 175−180.

(6) Maurice, V.; Salmeron, M.; Somorjai, G. A. The Epitaxial Growth of Zirconium on Pt(111) Single Crystal Surfaces. *Surf. Sci.* **1990**, *237*, 116−126.

(7) Meinel, K.; Schindler, K.-M.; Neddermeyer, H. Growth, Structure and Annealing Behaviour of Epitaxial ZrO_2 Films on Pt(111). *Surf. Sci.* **2003**, *532−535*, 420−424.

(8) Meinel, K.; Eichler, A.; Förster, S.; Schindler, K.-M.; Neddermeyer, H.; Widdra, W. Surface and Interface Structures of Epitaxial ZrO_2 Films on Pt(111): Experiment and Density-Functional Theory Calculations. *Phys. Rev. B* **2006**, *74*, No. 235444.

(9) Gao, Y.; Zhang, L.; Pan, Y. H.; Wang, G. D.; Xu, Y.; Zhang, W. H.; Zhu, J. F. Epitaxial Growth of Ultrathin $ZrO_2(111)$ Films on Pt(111). *Chin. Sci. Bull.* **2011**, *56*, 502−507.

(10) Antlanger, M.; Mayr-Schmölzer, W.; Pavelec, J.; Mittendorfer, F.; Redinger, J.; Varga, P.; Diebold, U.; Schmid, M. $Pt_3Zr(0001)$: A Substrate for Growing Well-Ordered Ultrathin Zirconia Films by Oxidation. *Phys. Rev. B* **2012**, *86*, No. 035451.

(11) Schnadt, J.; Knudsen, J.; Andersen, J. N.; Siegbahn, H.; Pietzsch, A.; Hennies, F.; Johansson, N.; Mårtensson, N.; Öhrwall, G.; Bahr, S.;

et al. The New Ambient-Pressure X-Ray Photoelectron Spectroscopy Instrument at MAX-Lab. *J. Synchrotron Radiat.* **2012**, *19*, 701−704.

(12) Weilach, C.; Kozlov, S. M.; Holzapfel, H. H.; Föttinger, K.; Neyman, K. M.; Rupprechter, G. Geometric Arrangement of Components in Bimetallic PdZn/Pd(111) Surfaces Modified by CO Adsorption: A Combined Study by Density Functional Calculations, Polarization-Modulated Infrared Reflection Absorption Spectroscopy, and Temperature-Programmed Desorption. *J. Phys. Chem. C* **2012**, *116*, 18768−18778.

(13) Rupprechter, G. Sum Frequency Generation and Polarization−Modulation Infrared Reflection Absorption Spectroscopy of Functioning Model Catalysts from Ultrahigh Vacuum to Ambient Pressure. *Adv. Catal.* **2007**, *51*, 133−263.

(14) Blöchl, P. E. Projector Augmented-Wave Method. *Phys. Rev. B* **1994**, *50*, 17953.

(15) Kresse, G.; Joubert, D. From Ultrasoft Pseudopotentials to the Projector Augmented-Wave Method. *Phys. Rev. B* **1999**, *59*, 1758−1779.

(16) Monkhorst, H. J.; Pack, J. D. Special Points for Brillouin-Zone Integrations. *Phys. Rev. B* **1976**, *13*, 5188−5192.

(17) Klimeš, J.; Bowler, D. R.; Michaelides, A. Van Der Waals Density Functionals Applied to Solids. *Phys. Rev. B* **2011**, *83*, No. 195131.

(18) Köhler, L.; Kresse, G. Density Functional Study of CO on Rh(111). *Phys. Rev. B* **2004**, *70*, No. 165405.

(19) Choi, J. I. J.; Mayr-Schmölzer, W.; Mittendorfer, F.; Redinger, J.; Diebold, U.; Schmid, M. The Growth of Ultra-Thin Zirconia Films on Pd₃Zr(0001). *J. Phys.: Condens. Matter* **2014**, *26*, No. 225003.

(20) Sun, Y. N.; Qin, Z. H.; Lewandowski, M.; Shaikhutdinov, S.; Freund, H. J. CO Adsorption and Dissociation on Iron Oxide Supported Pt Particles. *Surf. Sci.* **2009**, *603*, 3099−3103.

(21) Rupprechter, G.; Dellwig, T.; Unterhalt, H.; Freund, H. J. CO Adsorption on Ni(100) and Pt(111) Studied by Infrared−Visible Sum Frequency Generation Spectroscopy: Design and Application of an SFG-Compatible UHV−High-Pressure Reaction Cell. *Top. Catal.* **2001**, *15*, 19−26.

(22) Hopster, H.; Ibach, H. Adsorption of CO on Pt(111) and Pt6(111)×(111) Studied by High Resolution Electron Energy Loss Spectroscopy and Thermal Desorption Spectroscopy. *Surf. Sci.* **1978**, *77*, 109−117.

(23) Rupprechter, G.; Dellwig, T.; Unterhalt, H.; Freund, H. J. High-Pressure Carbon Monoxide Adsorption on Pt(111) Revisited: A Sum Frequency Generation Study. *J. Phys. Chem. B* **2001**, *105*, 3797−3802.

(24) Redhead, P. A. Thermal Desorption of Gases. *Vacuum* **1962**, *12*, 203−211.

(25) Kresse, G.; Gil, A.; Sautet, P. Significance of Single-Electron Energies for the Description of CO on Pt(111). *Phys. Rev. B* **2003**, *68*, No. 073401.

(26) Powell, C. J.; Jablonski, A. NIST Electron Inelastic-Mean-Free-Path Database. NIST Standard Reference Database 71, version 1.2; Gaithersburg, MD, 2010.

(27) Bakradze, G.; Jeurgens, L. P. H.; Mittemeijer, E. J. The Different Initial Oxidation Kinetics of Zr(0001) and Zr(1010) Surfaces. *J. Appl. Phys.* **2011**, *110*, No. 024904.

(28) Morant, C.; Sanz, J. M.; Galan, L.; Soriano, L.; Rueda, F. An XPS Study of the Interaction of Oxygen with Zirconium. *Surf. Sci.* **1989**, *218*, 331−345.

(29) De Gonzalez, C. O.; Garcia, E. A. An X-Ray Photoelectron Spectroscopy Study of the Surface Oxidation of Zirconium. *Surf. Sci.* **1988**, *193*, 305−320.

(30) Yeh, J. J.; Lindau, I. Atomic Subshell Photoionization Cross Sections and Asymmety Parameters: $1 \leq Z \leq 103$. *At. Data Nucl. Data Tables* **1985**, *32*, 1−155.

(31) Bakradze, G.; Jeurgens, L. P. H.; Mittemeijer, E. J. Valence-Band and Chemical-State Analyses of Zr and O in Thermally Grown Thin Zirconium-Oxide Films: An XPS Study. *J. Phys. Chem. C* **2011**, *115*, 19841−19848.

(32) Steininger, H.; Lehwald, S.; Ibach, H. Adsorption of Oxygen on Pt(111). *Surf. Sci.* **1982**, *123*, 1−17.

(33) Miller, D. J.; Öberg, H.; Kaya, S.; Sanchez Casalongue, H.; Friebel, D.; Anniyev, T.; Ogasawara, H.; Bluhm, H.; Pettersson, L. G. M.; Nilsson, A. Oxidation of Pt(111) under Near-Ambient Conditions. *Phys. Rev. Lett.* **2011**, *107*, No. 195502.

(34) Puglia, C.; Nilsson, A.; Hernnäs, B.; Karis, O.; Bennich, P.; Martensson, N. Physisorbed, Chemisorbed and Dissociated O₂ on Pt(111) Studied by Different Core Level Spectroscopy Methods. *Surf. Sci.* **1995**, *342*, 119−133.

(35) Kim, Y. S.; Bostwick, A.; Rotenberg, E.; Ross, P. N.; Hong, S. C.; Mun, B. S. The Study of Oxygen Molecules on Pt(111) Surface with High Resolution X-Ray Photoemission Spectroscopy. *J. Chem. Phys.* **2010**, *133*, No. 034501.

(36) Parkinson, C. R.; Walker, M.; McConville, C. F. Reaction of Atomic Oxygen with a Pt(111) Surface: Chemical and Structural Determination Using XPS, CAICISS and LEED. *Surf. Sci.* **2003**, *545*, 19−33.

(37) Hebenstreit, W.; Redinger, J.; Horozova, Z.; Schmid, M.; Podloucky, R.; Varga, P. Atomic Resolution by STM on Ultra-Thin Films of Alkali Halides: Experiment and Local Density Calculations. *Surf. Sci.* **1999**, *424*, L321−L328.